Geocarto International

ISSN: (Print) (Online) Journal homepage: https://www.tandfonline.com/loi/tgei20

Fracture aquifers identification in the Zou basin (West Africa) using remote sensing and GIS

Francis E. Oussou , Nicaise Yalo , Christopher E. Ndehedehe , Joseph Oloukoi , Abdoukarim Alassane , Moussa Boukari & Vinel H. G. Gbewezoun

To cite this article: Francis E. Oussou , Nicaise Yalo , Christopher E. Ndehedehe , Joseph Oloukoi , Abdoukarim Alassane , Moussa Boukari & Vinel H. G. Gbewezoun (2020): Fracture aquifers identification in the Zou basin (West Africa) using remote sensing and GIS, Geocarto International, DOI: 10.1080/10106049.2020.1852613

To link to this article: https://doi.org/10.1080/10106049.2020.1852613

GEOCARTO INTERNATIONAL
https://doi.org/10.1080/10106049.2020.1852613

Taylor & Francis
Taylor & Francis Group

REVIEW

Fracture aquifers identification in the Zou basin (West Africa) using remote sensing and GIS

Francis E. Oussou[a], Nicaise Yalo[a], Christopher E. Ndehedehe[b,c], Joseph Oloukoi[d], Abdoukarim Alassane[a], Moussa Boukari[a] and Vinel H. G. Gbewezoun[a]

[a]Laboratoire d'Hydrologie Appliquée, Institut National de l'Eau (INE), Université d'Abomey-Calavi, Cotonou, Bénin; [b]School of Environment & Science, Griffith University, Nathan, Queensland, Australia; [c]Australian Rivers Institute and Griffith School of Environment & Science, Griffith University, Nathan, Queensland, Australia; [d]African Regional Institute for Geospatial Information Science and Technology (AFRIGIST), Obafemi Awolowo University Campus, Ile-Ife, Nigeria

ABSTRACT

The riparian communities of the Zou basin of West Africa rely heavily on drinking water supplied by fractured aquifer systems. This study aims to provide accurate fracture maps and derived products (fracture density, coincidence map and cross-points) using Landsat 8 (visible and infrared bands) and PALSAR DEM datasets with borehole data collected from the national integrated database. Digital image processing techniques through image enhancement and directional Sobel filters application were used to analyse Landsat 8 and PALSAR data. Results show that the main orientations of fractures are N10-N20, N90-N100 and N180 for the visible, N10-N20, N40-N50, N90, N140 and N180 for the infrared and for the PALSAR DEM, they are N10-N20, N90-N100 and N170-N180. The fracture length overall interval is 0.15 to 21.2 km and the cumulative length of each fracture map is adjusted to power law with characteristic of exponent respectively 0.86, 0.91 and 0.96. The chi square (χ^2) test of cumulative length versus class frequency reveals a significant relationship for the visible and PALSAR fracture maps. Although, the calculated χ^2 is greater than the theoretical chi square for the infrared, there is a strong and positive correlation for the three fracture maps (0.94, 0.99 and 0.98). More than 50% of the fracture cross-points (CP) occurs with the North-South (NS) orientations. The coincidence map analysis shows that the PALSAR fracture map has the highest ratio of 0.88, proving it should prioritize over the visible and infrared maps. High flow ($Q > 5$ cubic m/h) boreholes located near the N10, N20 and N180 main orientations are more than 50% confirming their significant contribution to aquifers' productivity. The spatial and statistical analyses of these fractured aquifers are critical to improve drinking water access and water resources planning for the basin communities.

ARTICLE HISTORY
Received 24 June 2020
Accepted 27 October 2020

KEYWORDS
Drinking water; aquifer system; fracture map; groundwater flow; Zou basin

CONTACT F. E. Oussou francisoussou@gmail.com

Introduction

Aquifers are geological formations capable of bearing significant underground water flow depending on their geometric and hydrodynamic properties. The basement aquifers from the surface to the bottom consist of weathered layer and a bottom fractured layer that concentrates most of the groundwater (Biémi 1992; Savané 1997; Wyns et al. 2004; Lachassagne et al. 2011 cited by Tagnon et al. 2016). For the management and monitoring of these resources, remote sensing data offer an appropriate spectral and spatial resolution for better hydrogeological surveys (Bruning et al. 2009). Lineaments extraction through remote sensing technics has been recognized as an efficient way toward hydrogeological knowledge improvement because of the possibility to exhibit geological fractures that shelter groundwater (Das 1990) and even more structural elements enhancement from satellite images lead to a better geological accidents mapping (Youan Ta et al. 2008). Therefore, in bedrock areas, for example, different type of satellite images and aerial photographs have been used for multiple purposes such as groundwater potential evaluation and fractures network identification (Boukari 1982; Kouamé et al. 2009; Ndong et al. 2014; Yao et al. 2014; Assatse et al. 2016; Tagnon et al. 2016; Oussou et al. 2019). Furthermore, Remote sensing satellite observations such as Landsat 7 ETM + have been successfully used in the eastern Tauride belt (SE Turkey) to isolate hydrothermally altered rocks by applying the Crosta techniques (Aydal et al. 2007). This progress further highlights the importance of remote sensing as an emerging geospatial tool in hydrogeological and geophysical exploration studies.

Fractured aquifers cover more than 80% of the national territory of Benin republic and require a better understanding of their geometry for more reliable exploitation. For several decades, many authors have worked on this basement area in general and showed several proofs on the complexity of the geological formations and its richness with different types of minerals (e.g., Pougnet 1957; Bonhomme 1962; Okioh 1972; Boussari and Rollet 1974; Boukari 1982; Adissin Glodji 2012; d'Almeida et al. 2015). As the tectonic events affect the geology in different ways, the fractures network produced is either hydraulically active or has no hydrogeological interest (Lasm 2000). Fractures located beneath the weathered layer are challenging to be detected but geophysics, photo-interpretation and remote sensing methods provide significant information about their hidden geometries (Lasm 2000). Even more, Bourguet et al. (1980–1981) showed that there is a considerable correlation between the alteration thickness and the underlying fractured aquifer layer. From these evidences, the obvious recommendation to access aquifers in basement areas is to not only produce an accurate fracture maps but also analyse the existing boreholes lithology (20.5 ± 8.3 m) to identify high alteration thickness areas (Oussou et al. 2019).

Apart from low groundwater potential areas, drinking water supply in Benin (Figure 1) is essentially drawn from aquifers (Boukari 1998). Future projection of all water demand in 2025 shows that less than 18% of groundwater available and less than 40% of surface water will be required in the country (Vision Eau 2025, 1999). Therefore, there is no compelling water scarcity concern in a near future (Boukari 2002) but the increasing number of dried up and low productivity boreholes is an obvious challenge that water supply departments face daily. Furthermore, as the country is mainly covered by basement geological formations, the critical challenge remains aquifer's geometry and hydrodynamics properties evaluation for reliable borehole implantation. One of the ongoing governments' process-based initiatives in water sector is to move from smaller drinking water supply systems to bigger ones where many villages can benefit from the same water supply system managed by multi-national companies. In fact, this target to be reached

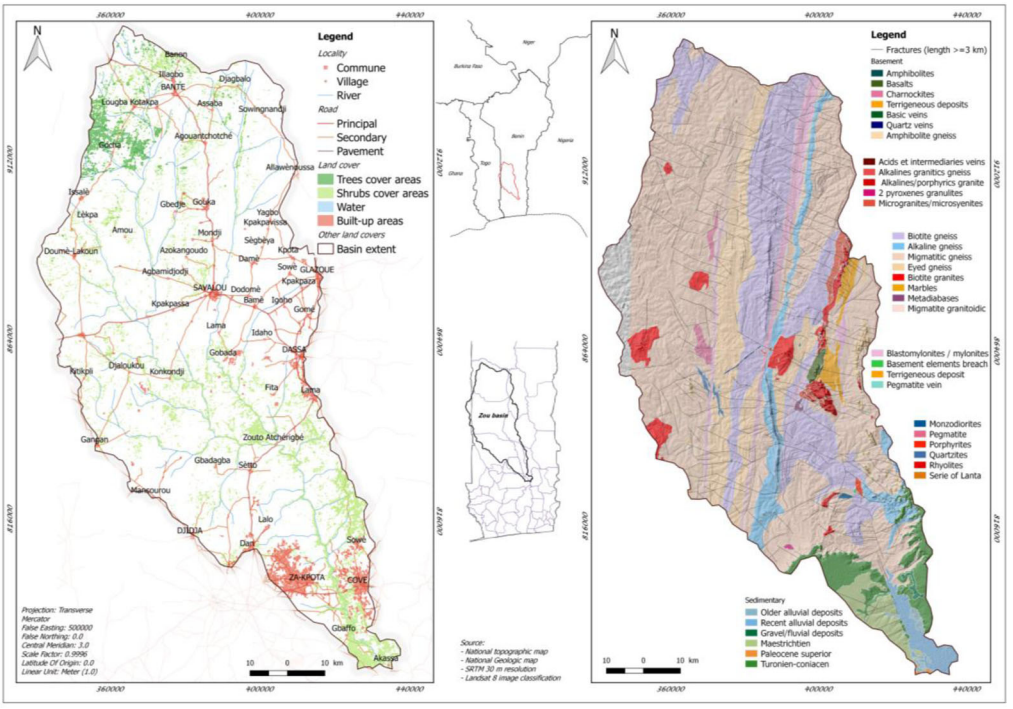

Figure 1. Geographical (left) and geological (right) maps of Zou basin.

requires highly productive aquifers which are not easy to be found in hard rock areas. The annual rainfall might be large enough, but the ratio of surface runoff and infiltration is clearly against aquifers recharge, which is a main parameter for sustainable water supply in the basin (Awoyé 2007). Aquifer systems across the world are indeed complex and understanding their groundwater–surface water interactions on a large-scale is even more difficult. Satellite gravity methods (e.g., Gravity Recovery and Climate Experiment) have emerged as new tools to study the response of aquifer and groundwater processes to the composite influence of extreme droughts and water extraction on a relatively larger scale (e.g., Ndehedehe et al. 2017; Ferreira et al. 2018; Ojha et al. 2019; Ndehedehe et al. 2020). However, knowledge on recharge and discharge mechanisms is still limited because of the coarse resolution of these satellite gravimetric methods. Considering complex recharge processes as noted here in Benin, new techniques to assess the status of aquifers and support reasonable management of groundwater resources for domestic application is crucial.

To fill some of these gaps in the Zou basin and also complement past studies in the region (Boukari 1982; Adissin Glodji 2012; Oussou et al. 2019), this study combines radar, and optical (infrared and visible remote sensing) datasets in a Geographical Information System (GIS) to provide a pattern for high productivity aquifers identification. The processing of satellite remote sensing image is employed to depict the hydrogeological conditions for better groundwater exploitation and decrease significantly the drinking water production cost in remote areas (Becker 2006; Dewandel et al. 2006; Meijerink 2007; Magesh et al. 2012).

In this study, the overarching goal is to update the catchment fracture map by integrating GIS with remote sensing techniques. To this end, secondary products such as fracture density, coincidence map and cross-points (CP) are derived. The aquifers hydrodynamic properties are analysed using GIS techniques in order to facilitate borehole implantation for drinking water supply. The methods, analyses and results are detailed and discussed in what follows.

Study area

Zou catchment is located between latitudes 7° and 8°33′ North and longitudes 1°35′ and 2°30′ East. At the latitude of Doume-Lakoun till Kitikpli, 2.2% of the basin covers the Togolese territory (Figure 1). Communes such as Savalou (31.0%) and Bantè (24.7%) are mainly represented. The basin is relatively well-watered as it is characterized by an intermediate climate between the subequatorial climate of the coast and the Sudano Sahelian one of the North parts of Benin (Bokonon-Ganta 1987; Boko 1988; Afouda 1990; Houssou 1998). The basin represents essentially an area where the influences of the monsoon from South-West and the continental trade winds also known as harmattan of the North-East are blurred. The rainfall evolves from 18.3 mm at the end of the year to 172.9 mm in July. Many studies such as Alidou et al. (1975), Boukari (1982), Breda (1985) and others show the high geological complexity of the area at the local and regional scale. Hence, the lithology and structure have been modified by several phases of deformation, metamorphism and magmatism. The basin surface is shaped by very old rocks dating from Precambrian (granite-gneissic basement).

The two geological map sheets (Breda 1989) that cover the entire basin exhibit the metamorphic complex represented by five types of gneiss such as the migmatite gneisses (mgn), eyed biotite gneisses (gno), amphibolite and biotite gneisses (gnab), alkaline and pyroxene gneisses (gnp) and biotite and hypersthene gneisses. The Kandi shear zone (KSZ), granomonzodioritic charnockites, which outcrop inside the migmatites, the marble and many other low proportion formations complete the list of the metamorphic rocks. Furthermore, the volcano-sedimentary series of Idaho-Mahou and Ouedo located, respectively, at the west and south of the study area (Figure 1) are composed of acid volcanic rocks (rhyolite and alkaline rhyolite), basic volcanic rocks (basalt and basaltic breccias) and also alkaline granites and microgranites (Boussari and Rollet 1974; Boukari 1982). Some of the major plication structures are related to the eyed gneisses, which radius of curvature is plurikilometric and the vertical axial plane direction is north-south from N10 to N30 (Breda 1989). The mylonitic bands cross the study area and are divided in three categories such as the western (N10), the central (N30) and the eastern band (N30). Consequently, the above-mentioned complexity governs the fracture maps spatial pattern whether in 2D or 3D and directly define the hydrogeological reservoirs flow occurrences.

Methodology

Data collected

Two scenes of 30 m spatial resolution in multispectral mode and 15 m in panchromatic mode were downloaded from the website https://earthexplorer.usgs.gov/ (Table 1). Spectral resolution of the Operational Land Imager-Thermal Infrared Sensors (OLI-TIRS) offers a possibility to evaluate the efficiency of the visible and infrared bands for lineaments identification in basement areas. The paths and rows are, respectively, 192-54 and 192-55 acquired on the 28 December 2014.

The radar dataset is from Advanced Land Observing Satellite-2 (ALOS-2) mission or Daichi-2 which is a next step of the radar (L-SAR) sensor launching program realised by the Japanese Aerospace Exploration Agency (JAXA). The polarimetric Phased Array L-band Synthetic Aperture Radar (PALSAR-L) including the 12.5 m spatial resolution ALOS PALSAR DEM has been used in this study to complete the visible and infrared bands as the goal of the study is to find the best dataset for lineaments extraction. The data is

Table 1. Satellite datasets characteristics.

Sensors	Name	Mode	Swath width	Bands (wavelengths)	Spatial/Temporal resolution
PALSAR	AP_07598_FBD_F0120_RT1 AP_07598_FBD_F0130_RT1 AP_07598_FBD_F0140_RT1 AP_07598_FBD_F0150_RT1 AP_07598_FBD_F0160_RT1 AP_08517_FBD_F0130_RT1 AP_08517_FBD_F0140_RT1 AP_08517_FBD_F0150_RT1	Dual polarization (HH and HV)	70 km	L ($\lambda = \sim$23.5 cm)	Pixel: 12.5 m
OLI-TIRS	LC81920552014362LGN00 LC81920542014362LGN00	–	185 km	Visible (B1–B5) and Infrared (B6–B7, B9–B11) Panchromatic (B8)	30 m and 15 m
MODIS/Terra	NOAA-AVHRR derived NDVI and EVI	–	–	36 bands	0.05°/16 day

Table 2. Sobel kernels in four directions (El-Sawy et al. 2016).

N-S			NE-SW			E-W			NW-SE		
Vertical edge detect			Right diagonal edge			Horizontal edge detect			Left diagonal edge		
−1	0	1	−2	−1	0	−1	−2	−1	0	1	2
−2	0	2	−1	0	1	0	0	0	−1	0	1
−1	0	1	0	1	2	1	2	1	−2	−1	0

downloaded from the Alaska Satellite Facility (ASF) Distributed Active Archive Center (DAAC) data portal (ASF DAAC 2015).

The Pira-Savè and Abomey-Zagnanado geological map sheets produced by Breda (1989) for 'Office Béninois des Mines' have been collected and georeferenced. Geological features such as fractures, shear zones, and geological formation outlines have been digitized. A total of 2371 boreholes data has been collected from the national database called 'Base de donnée Intégrée (BDI)'. This study uses mainly the boreholes' flow attribute to analyse fractured aquifers' hydrodynamic. For validation purpose, the National Oceanic and Atmospheric Administration-Advanced Very High Resolution Radiometer (NOAA-AVHRR) derived Normalized Difference Vegetation Index (NDVI) and Enhanced Vegetation Index (EVI) time series are also retrieved from an USGS website (https://lpdaac.usgs.gov/products/mod13a2v006/).

Lineaments identification

A lineament is any kind of linear feature, which can be found in a satellite image or aerial photography. The features are geological limits, slope ruptures, the river path, man-made structures and fracture network areas (Biémi 1992; Meijerink 2007; Bruning et al. 2009). The lineament detection operation starts with the image enhancement. Hence, the image quality is increased using one of the spatial domain methods (e.g., mode filter, median filter) or frequency domain methods like the Gaussian or Butterworth filter (Rahnama and Gloaguen 2014a, b). Stretching contrasts increase the tone distribution between elements in an image, and further lighten bright areas while dark regions become more darkened. Notably, lineaments detection filters are separated in three categories: gradient filters like Sobel (Table 2) and Prewitt, Laplacian filter (LOG) and optimal filter Canny. Differentiation, smoothing and labelling are applied to the filtered images to obtain the lineaments map (Marr and Hildreth 1980; Canny 1986; Deriche 1987; Ziou 1991 cited by Rahnama and Gloaguen 2014a, b; Stanislawski et al. 2018).

The visible and infrared bands (LANDSAT-8) are processed in remote sensing softwares (ENVI 5.1 and PCI Geomatica). The Principal Components and Convolution/Morphology filter tools are used to process both the visible and infrared stacked bands. The result of the Principal component 1 (PC 1) is then transferred to PCI Geomatica (PCI 2009) where the module 'LINE' algorithm (Table 3) is applied to extract the lineament features which in turn is converted into GIS well-known format shapefile for further spatial analysis. The trial version of PCI Geomatica software is used for semi-automatic linear features extraction and was made available after a request addressed to the software developer (http://www.pcigeomatics.com). The algorithm parameters are adapted to this study area based on the recommendation of Shankar et al. (2016) and El-Sawy et al. (2016).

According to Pirotti and Tarolli (2010), Tarolli et al. (2012), Persendt and Gomez (2016) and Niipele and Chen (2019), DEM features extraction, Earth Observation (EO) derived information will assist for better understanding of the environment and its

Table 3. Line module parameter values.

Parameters	Suggested value	Parameters	Suggested value
Filter radius (RADI)	50	Line fitting error threshold (FTHR)	7
Gradient threshold (GTHR)	100	Angular difference threshold (ATHR)	30
Length threshold (LTHR)	30	Linking distance threshold (DTHR)	50

operating systems such as fractured aquifers in this case. The steps for the PALSAR DEM processing consist of basic corrections, the Sobel filter application and lineaments extraction using the Line module. The directional filters Sobel highlight strong transitions reflectance and high spatial frequencies generally associated with lineaments. Four directions filters have been applied to the pre-processed bands.

Fractures' length statistical adjustment

The cumulative length (CL) of each fracture map is adjusted to the power law, which has been used in the past works (Jourda 2005; Koudou et al. 2013; Tagnon et al. 2016). Short fracture lengths (less than 1.28 km) are affected by the problem of 'Truncation' effect and the longer one (greater than 13.04 km) by 'censoring' effects (Ackermann et al. 2001; Zazoun 2008). Thus, the power law has been adjusted to the recommended interval ($1.28\text{km} \leq l \leq 13.04\text{km}$) and the chi square ($\chi^2$) test used to evaluate the relationship significance in the data.

$$C_t = a \times l^{\alpha}$$

with C_t : class frequency, a : proportionality coefficient and α : `characteristic.

Nearest neighbour analysis

The analysis concerns point-to-point and origin-to-point nearest neighbour statistic. The first ratio $(\hat{G}(h))$ has been calculated by dividing a nearest neighbour distance (l_i) sum from the ith centroid to the nearest one in a region by n the total number of points within a distance (h). The second one origin-to-point is an equivalent analysis where distance (l_i) from m random origins are compared to the nearest neighbours (Tran 2004).

$$\hat{G}(h) = \frac{1}{n} * \sum_{l_i \leq h} 1 \;\; or \;\; \hat{F}(h) = \frac{1}{m} * \sum_{l_i \leq h} 1$$

With ArcGIS tool 'Average Nearest Neighbour' (Figure 2), the fracture map from each satellite image is processed to evaluate the spatial pattern. For the PALSAR L-band extracted lineaments, the average nearest neighbour summary shows a clustered pattern and a very low z-score (-55.2) which means that there is less than 1% likelihood that the clustered pattern could be the result of random chance.

Fracture density and cross-points

Fracture density (FracDen) is formulated as total fracture length or counts per unit area (in 2D) or per unit volume (in 3D). This type of analysis is useful to find out major fracture populated area for high flow aquifers identification in hard rocks areas (Tran 2004). A CP is the point of intersection between fractures where groundwater flow occurrence might be very interesting for water supply (Tagnon et al. 2016). The open source software QGIS tool 'Line intersection' is used to generate the CPs.

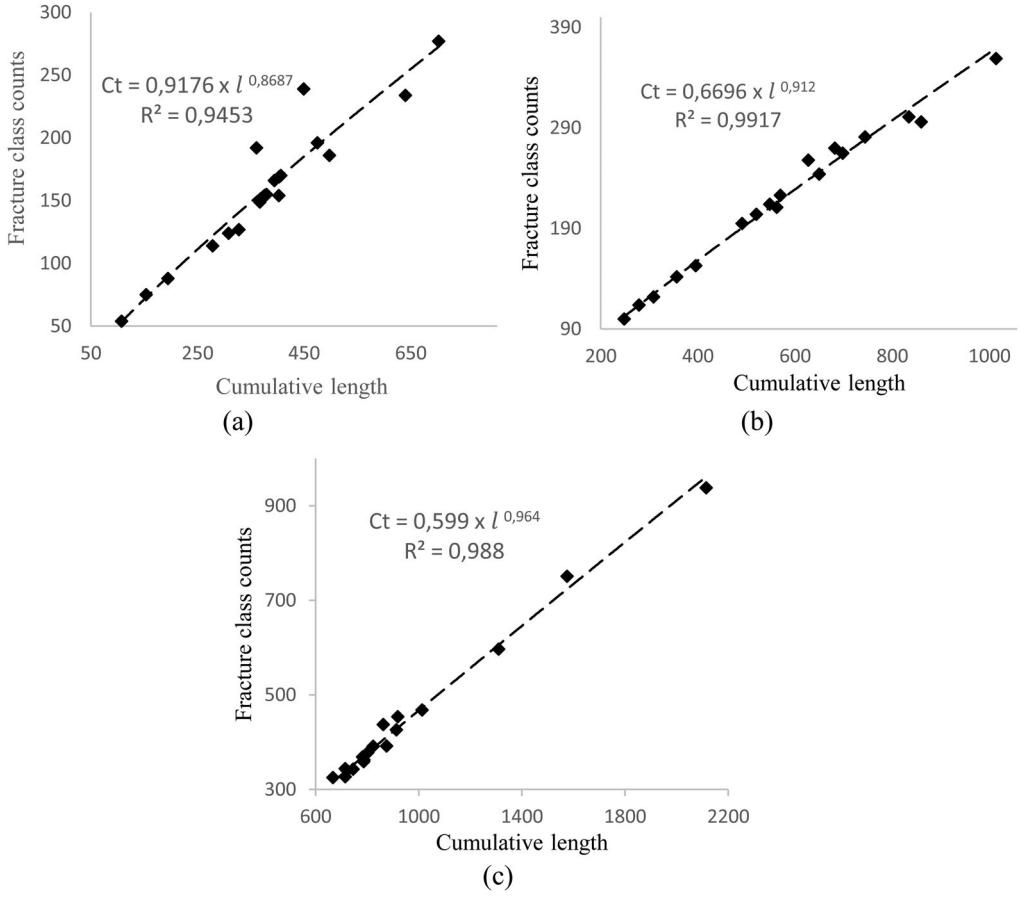

Figure 2. Cumulative length and class frequency regression of visible (a), Infrared (b) bands and PALSAR (c).

$$FracDen\ (2D) = \frac{2 * \sum_i Rad_i}{Model\ \ area}$$

$$FracDen\ (3D) = \frac{\pi * \sum_i (Rad_i)^2}{Model\ \ volume}$$

where $\sum_i Rad_i$ is the total fracture length or count.

Coincidence analysis

According to Magowe and Carr (1999), a lineament interpreted in two or more images is a coincident lineament. Groundwater prospecting in the basement areas requires a clear idea about the fracture network. Based on the works of Bruning et al. (2009) and Alonso-Contes (2011), the coincidence map provides a sure and consistent highlight of areas that have undergone tectonic actions where groundwater flows probably occur. In this study, three categories of spectral bands are considered to maximize the chance to retrieve the most accurate fracture map of the basin. The steps involved in this process are, to: (1) generate a buffer of acceptable size representing on average the zones of fractures, (2)

Table 4. Summary of statistical data for lineaments length and count.

Dataset	Count	Average	Standard deviation	χ^2
Visible	4595	1.89	1.15	61.46
Infrared	5344	2.2	1.4	21.91
PALSAR	31092	1.1	0.82	37.07

verify all the interpreted lineaments, (3) perform a GIS analysis to filter the interpretations and (4) analyse the performance of the coincidence map.

Guiraud and Alidou (1981), Boukari (1982), Adissin Glodji (2012) and several works undertaken in this basement are considered to have the size of the buffer. However, a detailed study on the width of the faults in the basin is missing. At the level of a fracture it is conceivable that the zone of influence is beyond the normal size of the fracture. The size of the buffers around the lineaments is then fixed at 200 m. The buffer generated from the three layers of lineaments are converted into raster format and reclassified into a binary image. The sum of the binary images gives the number of times the lineaments coincide and therefore the coincidence map of lineament is generated (Table 6). The minimum degree of coincidence is fixed at 2 to make the fracture map more accurate. The retained buffer area for a fracture map is divided by that of the total filtered area after overlapping the three fracture maps to obtain a ratio which in turn is used for ranking.

For the lineaments' coincidence validation purpose, the Normalized Difference Vegetation Index and Enhanced Vegetation Index time series derived from MODIS products MOD13A2 (Didan 2015) are used to compare the temporal change of vegetation greenness over areas mapped as coincidence areas and non-coincidence areas. A QGIS software extension called 'Temporal/Spectral Profile Tool' is used to extract the NDVI time series from the MODIS vegetation greenness dataset (a netcdf4 file format). After plotting, vegetation greenness turns out to be higher in the buffer zones. The principal component analysis (PCA, e.g., Jolliffe 2002) of the series is computed in order to identify the temporal pattern of the vegetation greenness trend from 2002 to 2019. The PCA is an extraction technique that reduces the dimensions of multivariate data by creating new sets of variables that are linear combinations of the original variable (e.g., Jolliffe 2002). Given that it helps to account for the most variability in the data (e.g., Ndehedehe et al. 2020), the method was used in this study to isolate dominant modes of orthogonal variability in vegetation greenness.

Results and discussion

Fracture maps statistics

The maps statistics reveal a minimum and maximum fracture length from 0.8 to 15.8 km for the visible, 0.3 to 21.2 km for the infrared and for the PALSAR image dataset from 0.15 to 11.2 km. The longest lineament is in granulite biotite gneiss (gngr) for the visible fracture map, in mainly amphibolite and biotite gneiss (gnab) for the infrared fracture map and for the PALSAR fracture map in alkalin gneiss (gnp). The infrared fracture map has the highest average and standard deviation (Table 4) meaning that it tends to depict high length fractures and there is an inconsistency in the distribution. The lowest length average and standard deviation are recorded on the PALSAR fracture map. The low standard deviation reveals a consistency of the fracture's length distribution and more, longer fractures are generally broken in smaller sub-orientations. In the case of the visible fracture map, the average and standard deviation are, respectively, 1.89 km and 1.15 km.

Table 5. Cross-points statistics.

Cross-points Intersections	Visible	Infrared	Palsar L
NS × EW	454	764	6582
NS × NESW	802	1095	4978
NS × NWSE	680	986	4686
EW × NESW	286	538	3586
EW × NWSE	247	457	3245
NESW × NWSE	552	1175	3218
Total	3021	5015	26295

For a significance level of 0.05 and a degree of freedom of 17, the calculated chi square (χ^2) for the visible and PALSAR fracture maps are greater than the theoretical χ^2. This means that the power law adjustment represents the significant relationship between the fracture length and class frequency per orientation. The calculated χ^2 for the infrared fracture map is less than the theoretical χ^2 value of 27.59. The fit test shows in this case that the distribution pattern is random and cannot be explained by any standard law.

The correlation coefficients of the three fracture maps are strong and positive, indicating values of 0.94, 0.99 and 0.98, respectively (Figure 2). This relationship is an indicator of how fracture abundance in an area can be revealing of the relatively high probability of significant groundwater flow. The adjustment to the power law gives a characteristic of exponent value of 0.86, 0.91 and 0.96, respectively for the visible, infrared and PALSAR.

Fracture intersections or cross-points (CP)

Each CP represents the intersection of two or more different orientation fractures. This is relevant for high flow borehole implantation in a basement area since groundwater flow occurs amid those weak areas. The geophysical technics such as vertical electric sounding (VES) can be directly performed at the location of these points. Some main fracture orientations such as the North-South associated to the Kandi Fault in the study area is highly revealed proving the maps accuracy. Furthermore, orientation category statistic of the geological features exhibits the prevailing type of CPs in each geological formation. For both the visible and PALSAR L dataset, the highest number of CPs and the second highest of the infrared dataset occur with the North-South (NS) orientation fractures respectively 802 CP, 6582 CP and 1095 CP (Table 5). This result suggests that for high flow borehole drilling in the basin, the NS orientation fractures are more likely to highlight significantly productive aquifers and should be privileged during geophysical field investigations. The lowest values recorded are 247 CP for the visible, 457 CP for the infrared and 3218 CP for the PALSAR L and each of them occurs with the NWSE orientations.

Regardless of the type of fracture map, the six types of CPs are represented in different proportions in the gneiss, granite, mylonites, quartzite and rhyolite (Figure 3). The most abundant CPs in the gneiss, mylonites, terrigenous deposits, charnockite and rhyolites alternates among the North-South East-West (NS × EW), North-South North-East South-West (NS × NESW) and North-South North-West South-East (NS × NWSE). This outcome narrows the fracture type to choose during high flow borehole investigations in these geological formations.

Orientation and spatial pattern

Figure 4 depicts the complexity of the fracture network orientations of the three datasets. The highest orientation frequencies occur for the Landsat visible fracture map on N10-N20, N90-N100 and N180. Each interval of orientation counts respectively for 16.4% with

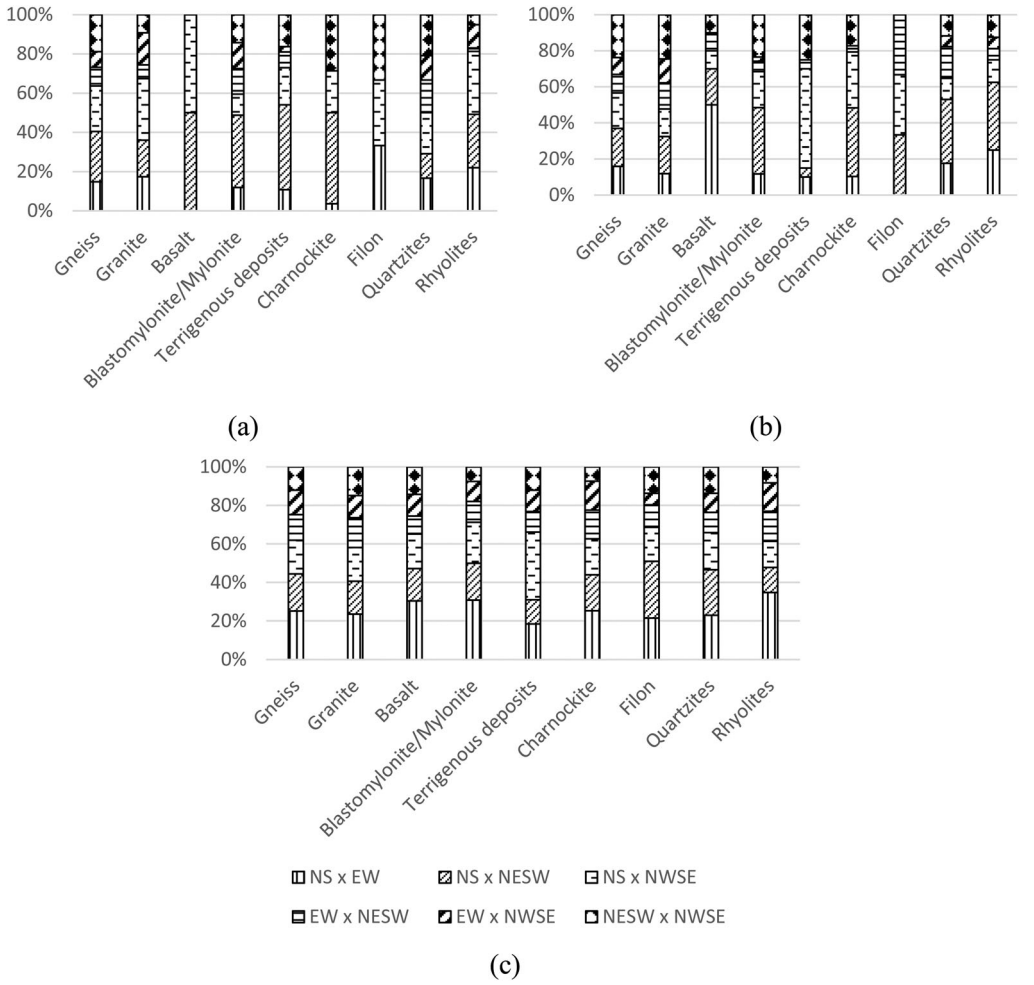

Figure 3. Cross-points versus geology for visible (a), infrared (b) and PALSAR (c) fracture maps.

Table 6. Fracture maps ranking.

Sensors/Source	Bands	Total buffer area at level 2 after overlapping (sqkm)	Retained buffer area (sqkm)	Ratio of retained area	Image rank
OLI - LANDSAT	Visible	2016.6	1027.7	0.51	3
TIRS - LANDSAT	Infrared		1377.4	0.68	2
Alos-2 PALSAR	PALSAR		1769.1	0.88	1

a cumulative length of 1426.7 km, 14.6% with a cumulative length of 1276.8 km and 8.8% for a cumulative length of 773.9 km. There is a frequency decrease trend from the North-South orientations (N10-N20 and N180) to the East-West (N90-N100) where a new peak is observed and a secondary orientation N50 with 6.7% of frequency and a cumulative length of 589.7 km.

The infrared fracture map shows main orientations such as N10-N20, N40-N50, N90, N140 and N180 (Figure 5). The frequency and cumulative length values are respectively 16.2% for 1928.5 km, 14.8% for 1755.9 km, 6.8% for 805.6 km, 6.4% for 764 km and 8.1% for 967.8 km. Furthermore, the PALSAR L band DEM indicates main orientations like N10-N20, N90-N100 and N170-N180. From this radar dataset the lineaments frequency

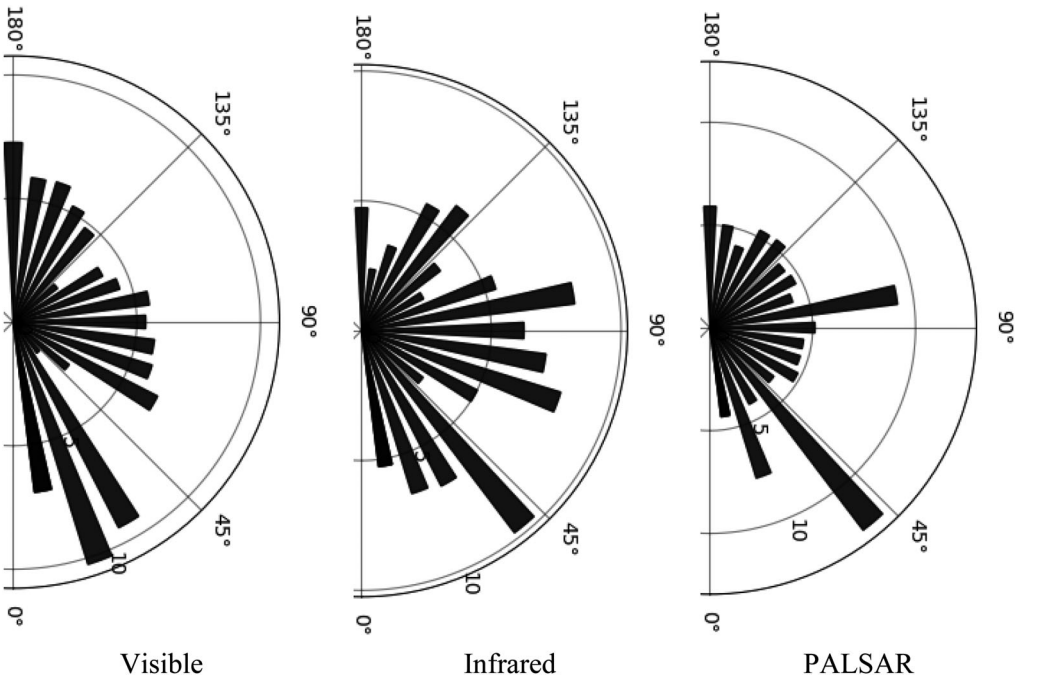

Figure 4. Lineaments length frequency (%).

and cumulative length are respectively 18.2% for 6024.9 km, 11.8% for 3916.4 km and 15.7% for 5216.5 km. Overall, the secondary orientation occurs on N30, N70-N80, N110-N120, and N160, which often connect the main orientations.

The Nearest Neighbour ratio for the visible fracture map is 0.72 with the observed and expected mean distance, respectively, of 0.64 km and 0.88 km (Figure 6). The infrared fracture map ratio is 0.80 with observed and expected mean distance of 0.66 km and 0.82 km and the PALSAR dataset ratio is 0.83 for observed mean distance of 0.29 km and expected distance 0.34 km. Given the z scores (−35.9, −26.9 and −55.2) and p values (0 for the three datasets), the lineaments extracted are therefore significantly aggregated.

The spatial distribution is therefore not random and shows that extracted lineaments are the result of diverse tectonic movements. In average, the highest density is 6.7 km/sqkm for the PALSAR fracture map and occurs in the quartzite formations and the lowest average is 5.5 km/sqkm recorded in the charnockite (Figure 7).

Coincidence map analysis

After overlapping the layers, the retained areas are 1027.7 sqkm for the visible fracture map, 1377.4 sqkm for the infrared and 1769.1 sqkm for the PALSAR (Table 6). According to the ratios, respectively, 0.51, 0.68 and 0.88, the PALSAR fracture map is the most accurate for weak geological areas identification in the basin (Figure 7). However, the Landsat visible and infrared fracture maps are interesting too and can be used when Synthetic Aperture Radar (SAR) bands are not available.

Figures 8 and 9 indicate that the NDVI and EVI series are greater in areas mapped as coincidence areas. In these areas, the NDVI mean and standard deviation are respectively 0.61 ± 0.14 against 0.57 ± 0.14 in non-coincidence areas. The EVI reveals the same picture with mean and standard deviation of 0.38 ± 0.12 against 0.36 ± 0.11. The mean comparison

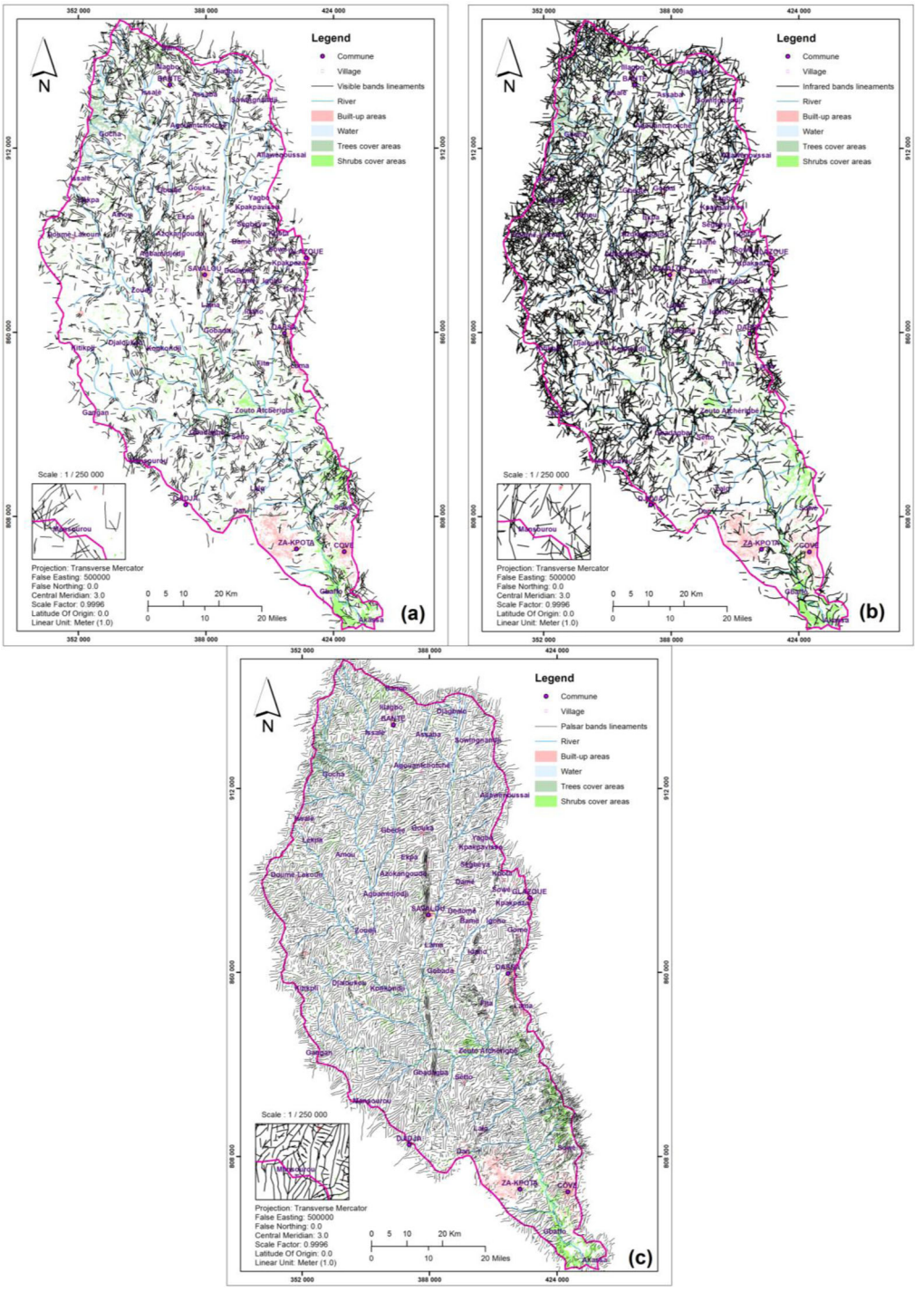

Figure 5. (a) Visible, (b) Infrared and (c) PALSAR DEM extracted fracture maps.

t-tests of the NDVI and EVI give, respectively, 2.95 and 2.18 with *p* values (0.003 and 0.029) smaller than 5% threshold. According to Allen (1998), vegetation growth and water availability have reciprocal effects on each other. Even more, water availability is

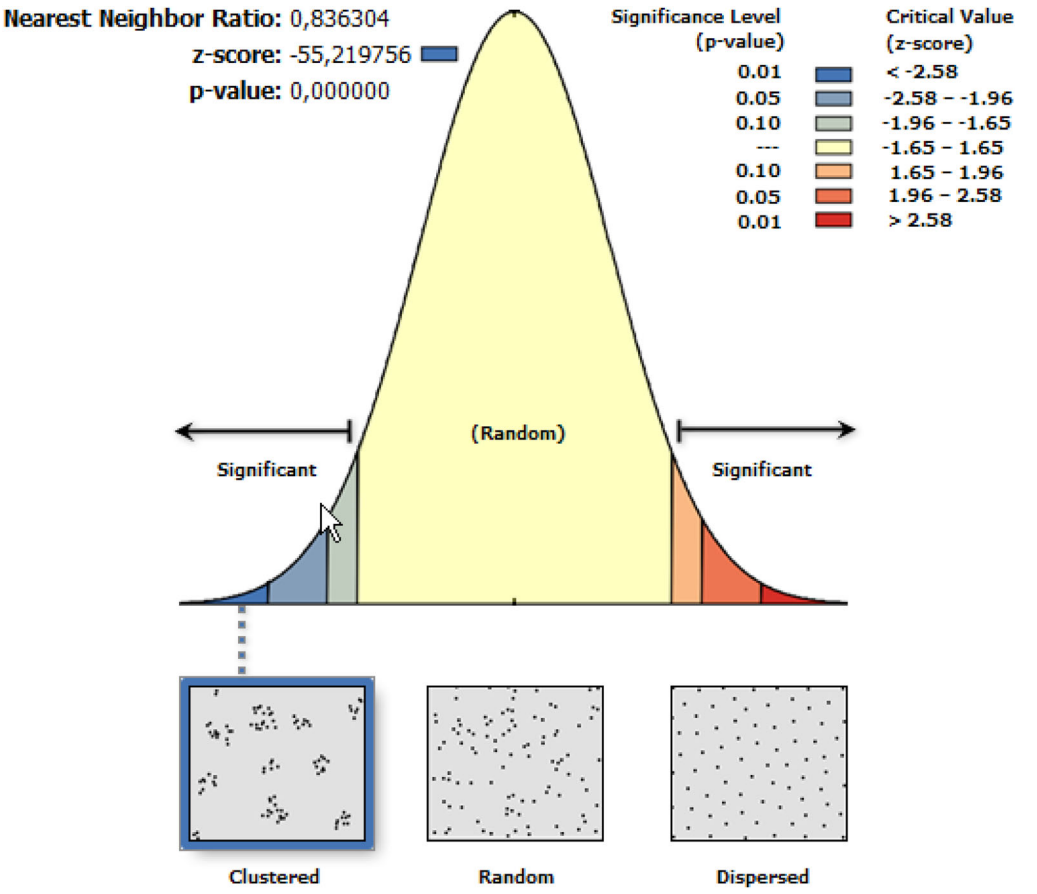

Figure 6. PALSAR L-band lineaments average nearest neighbour summary.

recognized as global driver for vegetation and indirectly affects the local drivers (Yang et al. 2009; Sandi et al. 2020).

Therefore, the evidence of higher vegetation greenness in the lineaments' coincidence areas could be an indicator of water resource availability for a longer time period. The series projection in different dimension through the principal component analysis (PC 1) reveals for both NDVI and EVI four trends from 2002 to 2019. The first uptrend starts from 2002 to 2008, the second downtrend from 2008 to 2013, the third uptrend from 2013 to 2016 and a recent downtrend occurring until 2019. In non-coincidence areas, each PC1 respond early to next unfolding change especially from 2012 to 2019. In contrary, the coincidence areas seem to be more resilient probably due to the higher vegetation greenness.

Fractured aquifers hydrodynamic

According to the organisation of 'Comité Interafricain d'Etude Hydraulique (C.I.E.H)', the classification shows globally that 37% of the boreholes has a very low flow (BRGM 1992). Whatever the geological formation (gneiss, granite, mylonites and terrigenous deposits), more than 50% of the boreholes has low flow to very low flow rate (Table 7). The percentage of high flow ones varies between 21.5% in granite and 28.6% in mylonites.

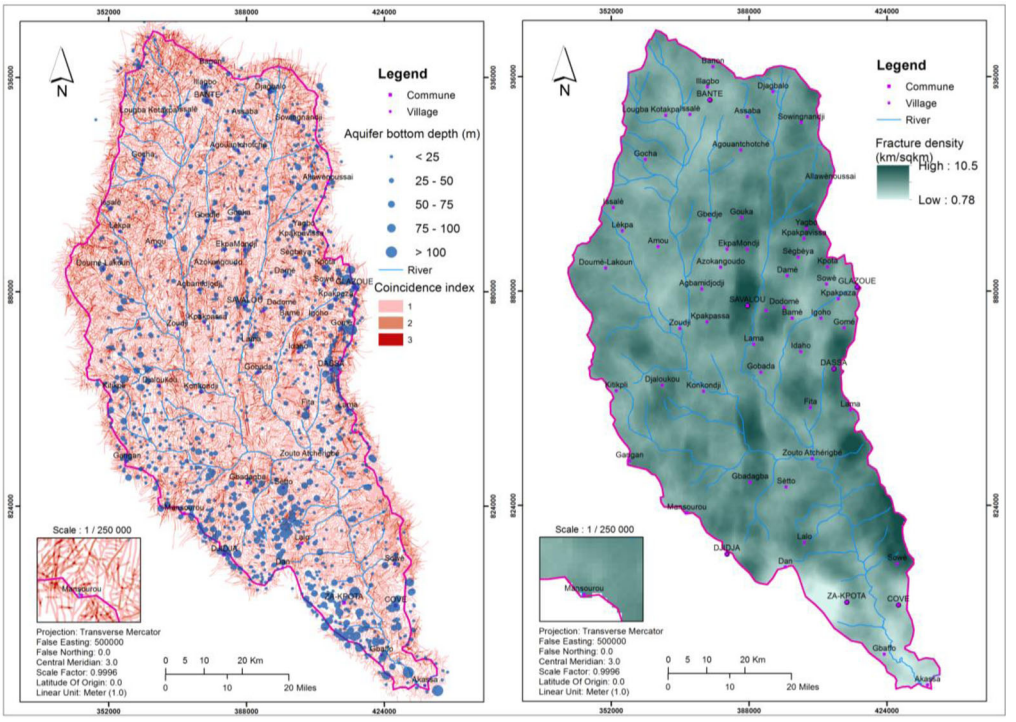

Figure 7. Coincidence (left) and fracture density (rigth) maps.

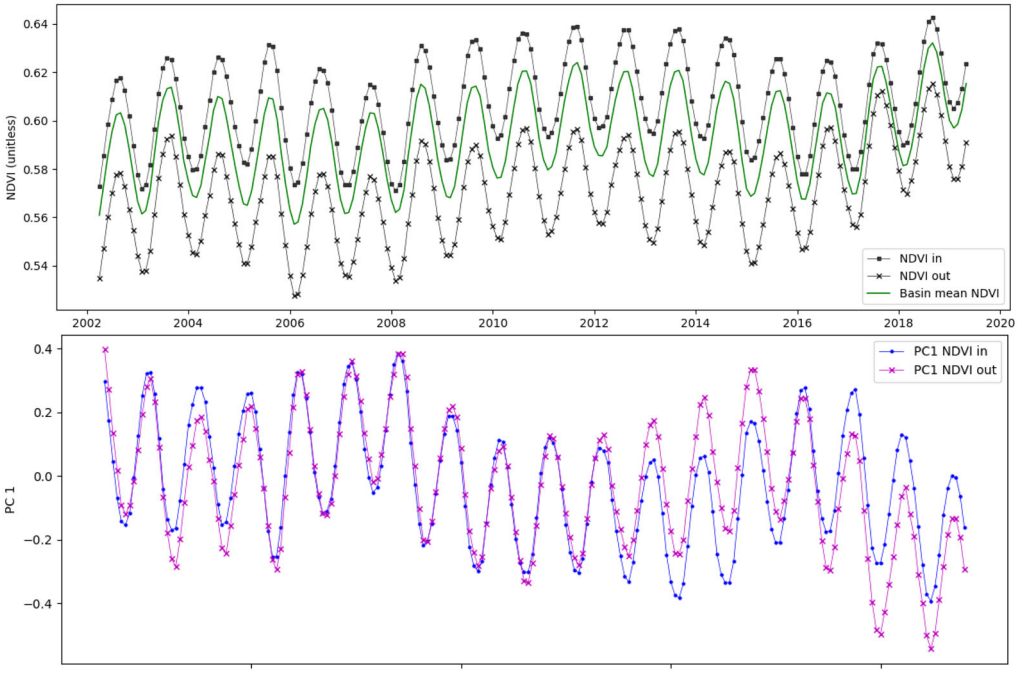

Figure 8. NDVI trends (upper) and first Principal component (lower) in coincidence and non-coincidence areas.

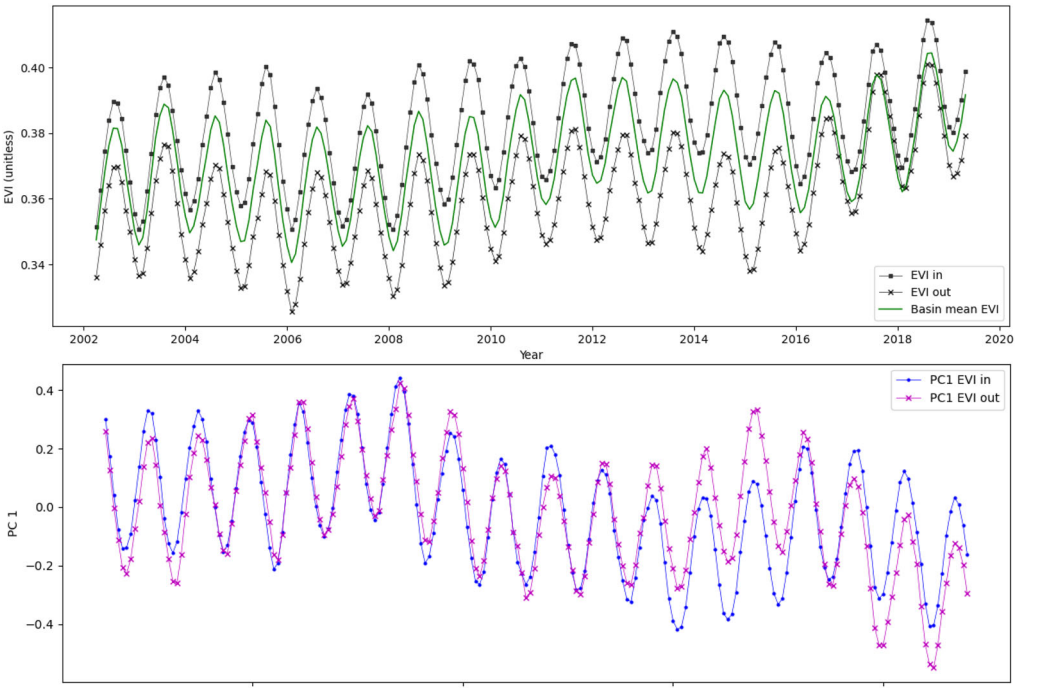

Figure 9. EVI trends (upper) and first Principal component (lower) in coincidence and non-coincidence areas.

Table 7. Flow classes versus geological formations.

Q (m^3/h)	Socle		Gneiss		Granite		Blastomylonites and mylonites		Terrigenous deposits	
0–1	680	37.0	605	37.3	24	30.4	25	39.7	17	35.4
1–2.5	464	25.3	400	24.6	31	39.2	15	23.8	7	14.6
2.5–5	294	16.0	265	16.3	7	8.9	5	7.9	13	27.1
>5	399	21.7	355	21.8	17	21.5	18	28.6	11	22.9
Totals	1837	100%	1625	100%	79	100%	63	100%	48	100%

According to the standard rules of Drinking Water Supply (Géohydraulique 1985), the flow of a positive borehole is greater or equal to 0.7 cubic meter per hour (Allé 2019). The percentage of negative borehole is 21% in the fractured reservoirs of the granite, 21% in the gneiss, 27% in the terrigenous deposits and 23% in the mylonites of Kandi shear zone (KSZ). As borehole drilling is difficult in the basin, a considerable number of negative boreholes are exploited by the population despite the low flow. The boreholes often dry up and are abandoned in favour of poor-quality sources of water like rivers.

2371 boreholes data are used to evaluate and assess the spatial groundwater flow characteristics based on the major orientations and CPs. It turns out that more than 50% of the high flow boreholes ($Q > 5$) are located near the N10, N20 and N180 (North-South) main orientations. These three fracture orientations are confirmed by each fracture map showing how abundant there are and how efficient there could be in drinking water supply for local communities. Further, although the N50, N90 and N100 might be named among the main fracture orientations, the percentage of high flow borehole identified is relatively low (Figure 10). The N50 orientation is revealed by the infrared fracture map only and the precedent evidence might be a further proof that groundwater investigations in the basin should consider the order of priority in the main orientations when looking for high flow groundwater occurrence areas. In the case of very low flow boreholes

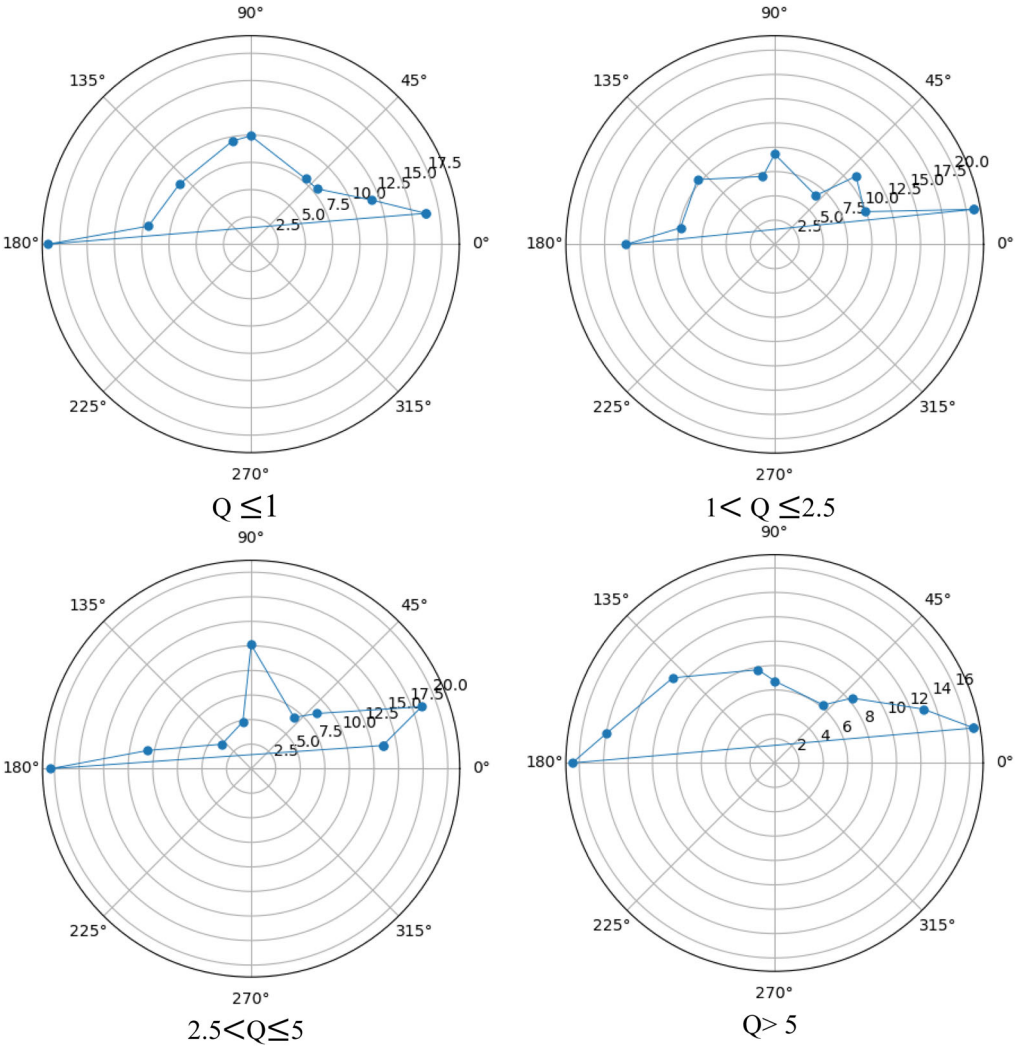

Figure 10. Flow classes versus main fracture orientations.

($Q \leq 1$), the distribution is almost same as in high flow boreholes, but it should be noticed that there is an increase in borehole percentage for the N50, N90 and N100. The type of CPs located near 38.9% of high flow and 33.3% of moderate flow (Table 8) boreholes is North-South North-West South-East (NS × NWSE). The highest percentage of the very low flow boreholes occurs on the North-South East-West (NS × EW), which represents the most abundant CPs type in the PALSAR fracture map.

Discussion

The hydrodynamics and aquifers geometry prospection in hard rock areas always require genuine understanding of their geologic tectonic conditions. In this basin, which is predominantly inhabited by people in rural communities, the fractures map accuracy availability appears to be critical for perennial groundwater access. Hence, three sources of dataset (Landsat 8 Visible/Infrared and PALSAR DEM) are processed using Remote

Table 8. Flow classes versus cross-points.

Cross-points	$Q \leq 1$	$1 < Q \leq 2.5$	$2.5 < Q \leq 5$	$Q > 5$
NS × EW	26.5	15.0	8.3	16.7
NS × NESW	21.9	10.0	25.0	11.1
NS × NWSE	17.9	25.0	33.3	38.9
EW × NESW	13.2	20.0	0.0	22.2
EW × NWSE	11.9	10.0	16.7	5.6
NESW × NWSE	8.6	20.0	16.7	5.6
Total	100%	100%	100%	100%

Sensing and Geographical Information System technique to come up with as accurate as possible fracture maps for better geophysical and hydrogeological field prospections. Basic statistics of the maps indicate that fracture networks derived from the ALOS-PALSAR DEM has the lowest average length (1.1 km) and a consistent distribution as the standard deviation of 0.82 km is less than the visible and infrared values, respectively, 1.15 km and 1.4 km. The spatial distribution across the basin depicts a repetitive pattern of longer fractures being broken in smaller one which is one of the reasons why the PALSAR fracture map count is higher. Whatever the visible (0.8 to 15.8 km), infrared (0.3 to 21.2 km) or PALSAR fracture map (0.15 to 11.2 km) is, the interval of length is in consistency with past studies (Jourda 2005; Baka 2012; Koudou et al. 2013, 2014; Lasm et al. 2004; Tagnon et al. 2016; Akokponhoué et al. 2019; Oussou et al. 2019). For the cumulative length adjustment, the calculated χ^2 for the visible and PALSAR fracture maps (61.46 and 37.07) are greater than the theoretical χ^2 revealing that there is a significant relationship between the cumulative length and class frequency. Although, the infrared fracture map calculated χ^2 is less than the theoretical χ^2, the power law adjustment for the three fracture maps gives in each case strong and positive correlation coefficients (visible 0.94, infrared 0.99 and PALSAR 0.98). A significant groundwater flow in a section of the basin therefore depends on the fracture length and the spatial distribution connectivity. The fractures length distribution is generally adjusted to the power law and this study corroborates works such as Bonnet et al. (2001), De Dreuzy et al. (2000) and Tagnon et al. (2016). According to Bonnet et al. (2001) and Darcel et al. (2003) cited in Tagnon et al. (2016), the exponent characteristic α of the power law and fracture density control the connectivity of the fracture media. The exponent characteristic obtained in this work are respectively 0.86, 0.91 and 0.96 and they appear to be outside the recommended interval ($2 \leq \alpha \leq 3$) in the literature.

The fracture CP distribution and density in a specific area can be obviously revealing of the fractured aquifer connectivity and underground water flow. Whatever the fracture map, the highest percentage of CPs occurs with the North-South (NS) orientation fractures respectively 64.1, 56.7 and 61.7%. Therefore, the NS orientation fractures should purposely be considered as there could highlight significantly productive aquifers. In the opposite side, the minimum number of CPs are 247 CP for the visible, 457 CP for the infrared and 3218 CP for the PALSAR. In this case, it turns out that the North-West South-East (NWSE) orientation fractures are the dominant. The geological formations such as gneiss, granite, mylonites, quartzite and rhyolite registered a significant percentage of the six CPs types. The North-South East-West (NS × EW), North-South North-East South-West (NS × NESW) and North-South North-West South-East (NS × NWSE) represent the general CPs spectrum in the gneiss, mylonites, terrigenous deposits, charnockite and rhyolites. Furthermore, for the PALSAR fracture map, the CPs spatial densities are 8 CP/sqkm in the rhyolites, 7 CP/sqkm in the basalt, 4 CP/sqkm in the quartzite, 3 CP/sqkm in the charnockite, 4 CP/sqkm in the granite, 2 CP/sqkm in the mylonites, 3 CP/sqkm in the gneiss and the terrigenous deposits.

Fracture rose diagrams of the maps reveal dominant orientation such as N10-N20, N90-N100 and N180 in the basin. The orientations frequency and cumulative lengths are in the case of the visible fracture map, respectively, 16.4% for 1426.7 km, 14.6% for 1276.8 km and 8.8% for 773.9 km, in the case of the infrared fracture map respectively 16.2% for 1928.5 km, 6.8% for 805.6 km and 8.1% for 967.8 km and finally in the case of the PALSAR fracture map respectively 18.2% for 6024.9 km, 11.8% for 3916.4 km and 15.7% for 5216.5 km. The N10-N20 and N180 represent a significant orientation in the central area of Benin republic especially the Kandi Shear Zone (KSZ) related to the pan-African orogenic cycle as recognized by many authors (Breda 1985; Adissin Glodji 2012; Alhassane et al. 2018). Further, it characterizes the crystallophyllian orientation of schistose green rocks, gneisses (NS to NNE-SSW, NNW-SSE), migmatites, and the extension of granite and spilite-keratophyre massifs (Boukari 1982; Breda 1989; Akokponhoué et al. 2019; Oussou et al. 2019). The secondary orientation N60, includes the NE-SW steering faults that affected the series of alkaline microgranites (Pougnet 1957 cited in Boukari 1982), the general orientation of the migmatites (N65) and the emplacement of the large batholiths of the porphyroid granite of Dassa-Zoumé. An ESE-NWN aplite injections close to the secondary directions N110-N120 have been confirmed in 'Lhoto' valley fractures. A fracture map spacing analysis using the Nearest Neighbour technic is a simple way to find out whether the fracture network is aggregated or randomly distributed. The ratios of the three fracture maps (respectively, 0.72, 0.80 and 0.83) and z scores (-35.9, -26.9 and -55.2) show that there is a significant spatial aggregation meaning that a tectonic geological movement have affected the formations. Based on the spatial density of the PALSAR fracture map, the Quartzite is more affected with a density of 6.7 km/sqkm and the charnockite is less affected recording 5.5 km/sqkm.

The coincidence map is a tool for better and more precise fracture identification. Therefore, the retained areas after buffer calculation and overlapping are 1027.7, 1377.4 and 1769.1 sqkm, respectively, for the visible, infrared and PALSAR. The PALSAR fracture map has the highest coincidence ratio of 0.88 which shows that the image gives a better accuracy compared to the visible and the infrared. The works of Bruning et al. (2009) and Alonso-contes (2011) carried out, respectively, in a volcanic terrain in Nicaragua and karst terrain in Puerto Rico corroborates this outcome. The radar dataset (ALOS PALSAR, Radarsat-1, Sentinel-1 …) and derived products (DEM, NDPI …) are given priority over optical images (Landsat-8, Sentinel-2) for accurate fracture identification. Although, this is the default trend, visible and infrared fracture maps can be interesting too when radar images are not available. The lineaments' coincidence areas evaluation using the NDVI and EVI series has proved their capacity to bear higher seasonal vegetation greenness compared to the non-coincidence areas which tend to react quickly to future unfolding changes. The NDVI and EVI mean comparison using t-tests have proved that there is significant difference as the p-values are less than the 5% threshold. The first principal component graphs depict two uptrends (2002–2008 and 2013–2016) and two downtrends (2008–2013 and 2016–2019) which show the climate temporal dynamic across the basin from vegetation greenness perspective. The temporal trend is to explain how water presence clues (ex. vegetation greenness, soil moisture, aquifers' discharge areas …) have changed comparing the "coincidence areas" to "non-coincidence areas". Figures 8 and 9 revealed that the "coincidence areas" have higher vegetation greenness (vegetation indexes) and are more resilient in dry season and to drought events (Principal Component Analysis).

Regardless of the geological context, at least 50% of the boreholes has a low flow to very low flow rate ($Q \leq 2.5$). Negative boreholes' percentage can reach overall 40% (Allé 2019) in the country basement area but there is an obvious change from one type of

geology to another one (terrigenous deposits 27%, mylonites of Kandi shear zone 23%, granite 21% and gneiss 21%). As aquifer's geometry and hydrodynamic appear to be very complex in the basin, borehole characteristics flip randomly. Comparing with past studies (Boukari 1982; Allé 2019; Oussou et al. 2019), the relatively low productivity of the fractured aquifers in the study area appear to be consistent. Although the low flow, boreholes are equipped for communities drinking water supply. In mylonites, high flow rate boreholes ($Q > 5$) reaches a high percentage of 28.6% and a lowest value of 21.5% is recorded in the granite. The hydrodynamic characteristics of a fractured aquifers after all depend on how intense the fracture density is both in 2D and 3D. From this perspective, the fracture maps reveal the surface 2D geometry and the existing borehole data offer valuable underground characteristics.

From borehole discharge versus orientation and CP perspective, near the N10, N20 and N180 (North-South) main orientations are located more than 50% of high flow boreholes. The presence of these orientations is key to find more easily productive aquifers in the basin. However, because of their abundance and the fact that the boreholes characteristics (discharge, depth, geographical position) depend mainly on communities drinking water needs, a non-negligible percentage of low flow boreholes is noticed. The N50, N90 and N100 are abundant too but located often near less productive boreholes. This evidence proves the order of priority which continues until the secondary classes of orientations. Furthermore, 38.9% of high flow and 33.3% of moderate flow boreholes are located near (200 m) the cross-points type North-South North-West South-East (NS × NWSE). Cross-points (CP) occurring with the NS orientations are more likely to reveal productive fractured aquifers. Two conditions prevailed in the basin. First, the borehole can be deep (around 80 m) and the flow rate does not increase with the depth (limited productivity): in this case, it usually ends in a dry or a weakly productive fracture. The second case is when the borehole is less deep (around 30 m) and productive: this second case, generally occurs when the precedent described conditions are met favouring safe drinking water supply.

Conclusions

Assessing the status of aquifers is crucial to supporting reasonable management of groundwater resources for domestic applications such as drinking. Understanding of aquifers' geometry in relation to drinking water access in basement environments through satellite images and groundwater hydrodynamic is therefore crucial. The Zou basin has a complex fracture network controlled by main orientations N10-N20, N90-N100 and N180, which define aquifers' geometry and secondary orientations N30, N70-N80, N110-N120, and N160. In this study, fracture maps derived products and statistics are made available for more efficient installations of boreholes. The cross-points, cumulative length and spatial density statistics depict the basin aquifers' 2D spatial pattern, which apprehension is critically required. Coincidence map obtained from the three fracture maps indicate the order of priority (ALOS-PALSAR DEM, Landsat Infrared and Landsat visible) when it comes to choosing the right satellite image. Existing borehole flow data combined with geology, main orientations and cross-points extend the analysis to better understanding of the prevailing groundwater flow system. Therefore, synergy between remote sensing communities and hydrogeologists will facilitate groundwater flow assessment, and the combined use of numerical models with remote sensing techniques and field data provides a platform to improve such understanding. Increased groundwater demand is often caused by a rise in human population and demands from industry and agriculture. Groundwater modelling that integrates remote sensing information and numerical models

could be useful in predicting surface deformations and other known impacts associated with extensive groundwater use. To achieve the Sustainable Development Goals (SDG) and reach a long-term reliable water supply in the basin, groundwater modelling of the fractured aquifers should be undertaken at local scale based on the above results and water pumping simulation performed for better future projection.

Acknowledgments

The authors are grateful to NASA and NOAA through ASF DAAC and EROS centers for all the satellite data and the National Department of Water Resources (DG-Eau) for borehole data used in this study. We also thank the reviewers for their valuable suggestions, which led to significant improvement of this manuscript.

Disclosure statement

No potential conflict of interest was reported by the author(s).

References

Ackermann RV, Schlische RW, Withjack M. 2001. The geometric and statistical evolution of normal fault systems: an experimental study of the effects of mechanical layer thickness on scaling laws. J Struct Geol. 23(11):1803–1819.

Adissin Glodji CL. 2012. La zone de cisaillement de Kandi et le magmatisme associé dans la région de Savalou-Dassa (Bénin): étude structurale, pétrologique et géochronologique. *Doctorat unique* des Universités Jean Monnet Saint-Etienne et d'Abomey-Calavi; France-Bénin; p. 260.

Afouda F. 1990. L'eau et les cultures dans le Bénin central et septentrional: étude de la variabilité des bilans de l'eau dans leurs relations avec le milieu rural de la savane africaine [Thèse de doctorat]. Université Paris IV Sorbonne.

Alidou S, Bard JP, Julien M. 1975. Conglomérats métamorphiques d'affinité tillique dans le socle dahoméen. 3e Réun. Ann. Sci. Terre, Mont-pellier, Fr., p. 6.

Allen R, Pereira L, Raes D, Smith M. 1998. Crop evapotranspiration guidelines for computing crop water requirements. FAO Irrig. Drain. Pap. 56, Food and Agric. Organ. of the U. N., Rome.

Akokponhoué YN, Yalo N, Akokponhoué HB, Youan TM, Agbahoungba G. 2019. Apport de la Télédétection et de la Géophysique dans la cartographie des fractures hydrauliquement actives en zone de socle au Centre-Ouest du Bénin. Eur Sci J. 15(27):426.

Alhassane I, Maman Sani AB, Issoufou S, Bachir SM, Boureima O. 2018. Apport des images ETM + et du Modèle Numérique de Terrain (MNT) à la Cartographie des fractures en région montagneuse: Secteur de Timia (Massif de l'Aïr. Eur Sci J. 14(9):1857–7881.

Allé IC. 2019. Évaluation de l'implantation géophysique des forages d'eau en zone de socle en milieu tropical (Bénin, Afrique de l'Ouest): apport de la tomographie de résistivité électrique pour la caractérisation de la cible hydrogéologique. *Thèse 3ème cycle*, Université d'Abomey-Calavi, Bénin.

Alonso-Contes CA. 2011. Lineament mapping for groundwater exploration using remotely sensed imagery in a karst terrain: Rio Tanama and Rio de Arecibo basins in the northern karst of Puerto Rico [Master's Thesis]. Michigan Technological University. http://digitalcommons.mtu.edu/etds/309.

ASF DAAC. 2015. ALOS PALSAR Radiometric Terrain Corrected low resolution; Includes Material © JAXA/METI 2007. Accessed through ASF DAAC 25 October 2016.

Assatse WT, Nouck PN, Tabod CT, Akame JM, Biringanine GN. 2016. Hydrogeological activity of lineaments in Yaounde Cameroon region using remote sensing and GIS techniques. Egypt J Remote Sens Space Sci. 19(1):49–60. http://dx.doi.org/10.1016/j.ejrs.2015.12.006.

Awoyé R. 2007. Modélisation du bilan hydrologique du bassin versant du Klou: contribution à la gestion durable des ressources en eau dans le Zou. [Thèse d'ingénieur] FSA/UAC, Bénin, p. 100.

Aydal D, Arda1 E, Dumanlilar Ö. 2007. Application of the Crosta technique for alteration mapping of granitoidic rocks using ETM + data: case study from eastern Tauride belt (SE Turkey). Int J Remote Sens. 28(17):3895–3913..

Baka D. 2012. Géométrie, hydrodynamisme et modélisation des réservoirs fracturés du socle protérozoïque de la région d'Oumé (Centre-Ouest de la Cote d'Ivoire) [Thèse Unique]. Univ. F.H. Boigny, Abidjan, Côte d'Ivoire, 249 p

Becker MW. 2006. Potential for satellite remote sensing of groundwater. Ground Water. 44(2):306–318.

Biémi J. 1992. Contribution à l'étude géologique, hydrogéologique et par Télédétection des bassins versants subsahéliens du socle précambrien d'Afrique de l'Ouest Hydrostructurale, hydrodynamique, hydrochimie et isotopie des aquifères discontinus des sillons et aires granitiques de la Haute Marahoué (Côte d'Ivoire). Thèse d'Etat Université Nationale de Côte d'Ivoire.

Boko M. 1988. Climat et communautés rurales au Bénin, rythmes climatiques et rythmes de développement. [Thèse de doctorat d'Etat]. Université de Bourgogne, Dijon, p. 605.

Bokonon-Ganta EB. 1987. Les climats de la région du Golfe du Bénin. (Afrique Occidentale). [Thèse de doctorat du 3ème cycle]. Paris IV, Sorbonne. p 248 + Annexes.

Bonhomme M. 1962. Contribution à l'étude géochronologique de la plate-forme de l'Ouest Africain. Ann. Fac. Sci. Univ. Clermont, v. 5. Gap: Louis-Jean; p. 60.

Bonnet E, Bour O, Odling NE, Davy P, Main IG, Cowie PA, Berkowitz B. 2001. Scaling of fracture systems in geological media. Rev Geophys. 39(3):347–383.

Boukari M. 1982. Contribution à l'étude hydrogéologique des régions de socle de l'Afrique intertropicale: l'hydrogéologie de la région de DASSA-ZOUME (Bénin). [Thèse 3ème cycle] Université Cheik Anta Diop Dakar; Sénégal; p. 140.

Boukari M. 1998. Fonctionnement du système aquifère exploité pour l'Approvisionnement en Eau de la ville de Cotonou sur le littoral Béninois. Impacte du développement urbain sur la qualité des ressources. [Thèse 3ème cycle]. Université cheik Anta Diop, Dakar, Sénégal, p. 256.

Boukari M. 2002. Réactualisation des connaissances hydrogéologiques relatives au bassin sédimentaire côtier du Bénin. Direction de l'Hydraulique, Cotonou, p. 3–134.

Bourguet L, Camerlo J, Fahy JC, Vailleux Y. 1980–1981. Méthodologie de la recherche hydrogéologique en zone de socle cristallin. Bull. B.R.G.M. Sér. II, Sect. III, n°. 4; pp. 311–324.

Boussari W, Rollet M. 1974. Découverte d'un bassin volcano-sédimentaire dans la région Centre-Ouest du Dahomey. C R Acad Sci. 279:29–32.

Breda. 1985. Etude de la cartographie géologique et prospection minière de reconnaissance au Sud du 9ème parallèle. Première phase.

Breda. 1989. Notice explicative de la carte géologique à 1/200000. Feuilles Pira-Savè, Abomey-Zagnanado, Lokossa-Porto-Novo. p. 77.

BRGM 1992. Document – Guide pour l'implantation et la mise en exploitation des forages à gros débit en zone de socle cristallin. *Rapport C.I.E.H,* Octobre 1992. p88 + Annexes.

Bruning JN, Gierke JS, Maclean AL. 2009. Digital processing and data compilation approach for using remotely sensed imagery to identify geological lineaments in hard-rock terrains: an application for groundwater explorations in Nicaragua. ASPRS 2009 Annual Conference Baltimore, Maryland, March 9–13.

Canny JA. 1986. Computational approach to edge detection. IEEE Trans Pattern Anal Mach Intell. 8(6): 679–698.

Das D. 1990. Satellite remote sensing in subsurface water targeting. In *Proceeding ACSM-ASPRS Annual Convention*. pp. 99–103.

Darcel C, Bour O, Davy P, De Dreuzy JR. 2003. Connectivity properties of two dimensional fracture networks with stochastic fractal correlation. Water Resour Res. 39(10):1272–1285.

D'Almeida GAF, Yessoufou S, Chala D, Obossou L. 2015. Caractéristiques pétrographiques et structurales des calcaires du département du Zou, sud du Bénin. Afrique Sci. 11(6):139–157.

De Dreuzy JR, Davy P, Bour O. 2000. Percolation parameter and percolation-threshold estimates for three-dimensional random ellipses with widely scattered distributions of eccentricity and size . Phys Rev E Stat Phys Plasmas Fluids Relat Interdiscip Topics. 62(5 Pt A):5948–5952.

Deriche R. 1987. Using Cannys criteria to derive a recursively implemented optimal edge detector. Int J Comput Vision 1:167–187.

Dewandel B, Lachassagne P, Wyns R, Marechal JC, Krishnamurthy NS. 2006. A generalized hydrogeological conceptual model of granite aquifers controlled by single or multiphase weathering. J Hydrol. 330(1–2):260–284.

Didan K. 2015. MOD13Q1 MODIS/Terra Vegetation Indices 16-Day L3 Global 250m SIN Grid V006. NASA EOSDIS Land Processes DAAC. [Accessed 2020 Aug 27]. https://doi.org/10.5067/MODIS/MOD13Q1.006.

El-Sawy K, Atef MI, El-Bastawesy MA, El-Saud WA. 2016. Automated, manual lineaments extraction and geospatial analysis for Cairo-Suez district (Northeastern Cairo-Egypt), using remote sensing and GIS. IJISET. 3(5):491–500.
Ferreira V, Montecino H, Ndehedehe C, Heck B, Gong Z, Westerhaus M, de Freitas S. 2018. Space-based observations of crustal deflections for drought characterization in Brazil. Sci Total Environ. 644: 256–273.
Houssou CS. 1998. Les bioclimats humains de l'Atacora (Nord-Ouest du Bénin) et leurs implications socio-économiques. Thèse pour l'obtention du grade de Docteur de l'Université de Bourgogne.
Jourda JPR. 2005. Méthodologie d'application des techniques de télédétection et des systèmes d'information géographique à l'étude des aquifères fissurés d'Afrique de l'Ouest. Concept de l'hydrotechnique spatiale: cas des zones tests de la Côte d'Ivoire. [Thèse de Doctorat d'Etat ès Sciences Naturelles]. Univ. Cocody (Abidjan, Côte d'Ivoire).
Géohydraulique 1985. Notice descriptive de la carte Hydrogéologique du Bassin Sédimentaire Côtier du Bénin à l'échelle 1/200 000è.
Guiraud R, Alidou S. 1981. La faille de Kandi (Bénin), témoin du rejeu fini-crétacé d'un accident majeur à l'échelle de la plaque africaine. C.R. Acad. Sci., Paris, t. 293:7779–7782.
Jolliffe IT. 2002. Principal component analysis. Springer Series in Statistics, 2nd ed. New York: Springer.
Kouamé KF, Lasm T, Saley MB, Tonyé E, Bernier M, Wade S. 2009. Extraction linémentaires par morphologie mathématique sur une image RSO de RADARSAT-1: application au socle Archéen de la Côte d'Ivoire. *Journées d'Animation Scientifique* (JAS09) de l'AUF, Alger Novembre 2009.
Koudou A, Lasm T, Kouame KF, Youan Ta M, Assoma TV, Biémi J. 2013. Contribution des images aster à la connaissance des aquifères fracturés de la région de Duékoué (Ouest de la Cote d'Ivoire). Photo-Interprétation. Eur J Appl Remote Sens. 2012/4:48–66.
Koudou A, Assoma TV, Adiaffi B, Youan Ta M, Kouamé KF, Lasm T. 2014. Analyses statistique et géostatistique de la fracturation extraite de l'imagerie ASAR ENVISAT du Sud-Est de la Côte d'Ivoire. Larhyss J. 20:147–166.
Lasm T, Kouamé KF, Soro N, Jourda JPR, Biémi J. 2004. Analyse géostatistique de la fracturation extraite de l'imagerie spatiale aeroportée et satellitaire. Application à la région de Man-Danané (Ouest de la Côte d'Ivoire). Rev Ivoir Sci Technol. 5:135–154.
Lasm. 2000. Hydrogéologie des réservoirs fracturés de socle : analyses statistique et géostatistique de la fracturation et des propriétés hydrauliques. Thèse unique. Univ. Poitiers (France). 233p.
Lachassagne P, Wyns R, Dewandel B. 2011. The fracture permeability of Hard Rock Aquifers is due neither to tectonics, nor to unloading, but to weathering processes. Terra Nova. 23(3):145–161.
Magesh NS, Chandrasekar N, Soundranayagam JP. 2012. Delineation of groundwater potential zones in Theni district, Tamil Nadu, using remote sensing, GIS and MIF techniques. Geosci Front. 3(2): 189–196.
Magowe M, Carr JR. 1999. Relationship between lineaments and ground water occurrence in western Botswana. Ground Water. 37 (2):282–286.
Marr D, Hildreth E. 1980. Theory of edge detection. Proc R Soc Lond Ser B Biol Sci. 207:187–217.
Meijerink AMJ. 2007. Remote sensing applications to groundwater. IHP-VI, series on groundwater no. 16. UNESCO.
Ndong BF, Ntomba SM, Messi EJ, Okia D, Mvondo JO. 2014. Définition structurale des linéaments par traitement d'image satellitaire: cas du massif de Ngovayang (Sud Cameroun). Afr Sci. 10(3):107–112. ISSN 1813-548X
Ndehedehe CE, Awange J, Kuhn M, Agutu N, Fukuda Y. 2017. Climate teleconnections influence on West Africa's terrestrial water storage. Hydrol Process. 31 (18):3206–3224..
Ndehedehe CE, Burford MA, Stewart-Koster B, Bunn SE. 2020. Satellite-derived changes in floodplain productivity and freshwater habitats in northern Australia (1991–2019). Ecol Indic. 114 (2020):106320..
Niipele JN, Chen J. 2019. The usefulness of ALOS-PALSAR DEM data for drainage extraction in semi-arid environments in The Iishana sub-basin. J Hydrol: Reg Stud. 21:57–67. doi.org/
Ojha C, Werth S, Shirzaei M. 2019. Groundwater loss and aquifer system compaction in San Joaquin Valley during 2012-2015 Drought. J Geophys Res Solid Earth. 124(3):3127–3143..
Okioh L. 1972. Contribution à l'étude morphologique des reliefs résiduels de la région de Dassa-Zoumé, Fita et Savalou (Dahomey). [Thèse de doctorat], Université de Paris VII, Paris, p. 163.
Oussou EF, Oloukoi J, Yalo N, Boukari M. 2019. Analyse Spatiale du potentiel en eau souterraine dans le bassin du Zou au Sud du Benin (Afrique de L'ouest). Eur Sci J. 15(27):1857–7881.
PCI 2009. Geomatica Version 10.3 User's Manual. Richmond Hill, ON: PCI Geomatics Enterprises.

Persendt FC, Gomez C. 2016. Assessment of drainage network extractions in a low-relief area of the Cuvelai Basin (Namibia) from multiple sources: LiDAR, topographic maps, and digital aerial orthophotographs. Geomorphology. 260:32–50.
Pirotti F, Tarolli P. 2010. Suitability of LiDAR point density and derived landform curvature maps for channel network extraction. Hydrol Process. 24 (9):1187–1197. doi.org/
Pougnet RS. 1957. Le Précambrien du Dahomey. Bull. Dir. fédér. Min. Afr. occ. fr. Dakar.
Rahnama M, Gloaguen R. 2014a. TecLines: A MATLAB-Based Toolbox for Tectonic Lineament Analysis from Satellite Images and DEMs, Part 1: Line Segment Detection and Extraction. Remote Sens. 6(7): 5938–5958. ISSN 2072–4292.
Rahnama M, Gloaguen R. 2014b. TecLines: A MATLAB-based toolbox for tectonic lineament analysis from satellite images and DEMs, Part 2: line segments linking and merging. Remote Sens. 6(11): 11468–11493. ISSN 2072–4292.
Sandi SG, Saco PM, Rodriguez JF, Saintilan N, Wen L, Kuczera G, Riccardi G, Willgoose G. 2020. Patch organization and resilience of dryland wetlands. Sci Total Environ. 726:138581..
Savané I. 1997. Contribution à l'étude géologique et hydrogéologique des aquifères discontinus du socle cristallin d'Odienné (Nord-Ouest de la Côte d'Ivoire). Apport de la télédétection et d'un système d'information géographique à référence spatiale. [Thèse de Doctorat d'Etat ès Sciences Naturelles]. Univ. Cocody (Côte d'Ivoire). p. 332.
Shankar B, Tornabene LL, Osinski GR, Roffey M, Bailey JM, Smith D. 2016. Automated lineament extraction technique for the Sudbury impact structure using remote sensing datasets- an update. *47th Lunar and Planetary Science Conference*. p. 2.
Stanislawski LV, Survila K, Wendel J, Liu Y, Buttenfield BP. 2018. An open source high-performance solution to extract surface water drainage networks from diverse terrain conditions. Cartogr Geogr Inf Sci. 45 (4):319–328. doi.org/
Tagnon BO, Lasm T, Douagui AG, Savané I. 2016. Statistical and geostatistical analysis of lineaments network mapped in the Precambrian basement: Case of Divo-Oume Region (Southern Cote d'Ivoire). Eur Sci J. 12(33):299.
Tarolli P, Giulia S, Dalla Fontana G. 2012. Geomorphic features extraction from high-resolution topography: landslide crowns and bank erosion. Nat Hazards. 61(1):65–83. doi.org/
Tran NH. 2004. Characterisation and modelling of naturally fractured reservoirs [PhD. Thesis]. Sydney, Australia: University of New South Wales. p. 227.
Vision Eau Bénin. 1999. Vision Eau Bénin 2025. Document final, Décembre 1999.
Wyns R, Baltassat JM, Lachassagne P, Legtchenko A, Vairon J. 2004. Application of proton magnetic resonance soundings to groundwater reserves mapping in weathered basement rocks (Brittany, France). Bull. Soc. Géol. Fr. 175:21–34.
Yang D, Shao W, Yeh PJ, -F, Yang H, Kanae S, Oki T. 2009. Impact of vegetation coverage on regional water balance in the nonhumid regions of China. Water Resour Res. 45(7): W00A14.
Yao KT, Oga M-S, Kouadio KE, Fouché O, Ferriere G, Pernelle C. 2014. Rôle hydrogéologique des linéaments structuraux en milieu cristallin et cristallophyllien: cas du bassin versant du Sassandra, Sud-Ouest de la Côte d'Ivoire. Afr Sci. 10(4):78–92. ISSN 1813-548X
Youan Ta M, Lasm T, Jourda JP, Kouamé KF, Moumtaz R. 2008. Cartographie des accidents géologiques par imagéries satellitaire Landsat-7 ETM + et analyse des réseaux de fractures du socle précambrien de la région de Bondoukou (Nord-Est de la Côte d'Ivoire). Télédétection, Editions Scientifiques GB. 8(2): 119–135.
Zazoun RS. 2008. The Fadnoun area, Tassili-n-Azdjer, Algeria: Fracture network geometry analysis. J Afr Earth Sci. 50°(5) :273–285.
Ziou D. 1991. Line detection using an optimal IIR filter. Pattern Recognit. 24(6):465–478.